3

Materials for Acoustic Wave Generation and Modulation

Noé Jiménez

Universitat Politècnica de València, Instituto de Instrumentación para Imagen Molecular, Camino de Vera s/n, València 46022, Spain

3.1 Introduction

3.1.1 Generation and Detection of Ultrasound

Acoustic waves have been used in medicine since the times of Hippocrates of Kos in fifth century BCE, when the sounds of the body were listened through auscultation during a physical examination. However, since the last century, modern technologies for acoustic wave detection, and also generation, have enabled more reliable medical imaging techniques, which are now common in the clinical practice. These include standard ultrasound imaging and a broad spectrum of acoustic imaging modalities such as Doppler ultrasound to detect flow speed, ultrasound elastography to measure tissue elasticity, quantitative ultrasound to evaluate bones, contrast ultrasound imaging to enhance ultrasound sensitivity and specificity, and, recently, functional ultrasound imaging to measure brain activity, ultrasound localization microscopy to image blood vessels at super resolution, or photo-acoustic techniques to provide molecular imaging, among others.

Beyond imaging, when the intensity of the acoustic waves is increased, intense vibrations can induce biological effects on tissue. In this way, focused ultrasound is emerging as a therapeutic modality with a whole branch of promising modalities. These include now classical treatments for kidney stone fragmentation using extracorporeal shock wave lithotripsy, high-intensity focused ultrasound to locally ablate tissue through thermal effects, emerging local drug delivery applications such as sonodynamic therapy, sonoporation, or blood-brain barrier opening, or promising therapeutic applications such as histotripsy to mechanically destroys tissue through cavitation creating a lesion with very sharp boundaries. In addition, a broad range of ultrasound transducers are used as biomedical tools such as ultrasonic baths for cleaning and sterilization of medical and surgical instruments, sonotrodes for ultrasonic processing and sonochemistry, and a wide range of ultrasonic motors, actuators and sensors in medical instrumentation.

Acoustic Technologies in Biology and Medicine, First Edition.
Edited by Adem Ozcelik, Ryan Becker, and Tony Jun Huang.
© 2024 WILEY-VCH GmbH. Published 2024 by WILEY-VCH GmbH.

3.1.2 Technologies for Ultrasound Transducers

At the root of these biomedical applications is the generation and detection of acoustic waves using a transducer, i.e. a device that converts an electric signal into a mechanical vibration to generate an acoustic wave, and, typically, they can also generate an electric signal when detecting an acoustic or elastic wave. There exists several technologies to convert mechanical to electrical energy, including piezoelectric transducers (based on the piezoelectricity of the materials), magnetostrictive transducers (based on the magnetostriction of ferromagnetic materials), capacitive micromachined ultrasonic transducers (CMUT, based on capacitive microelectromechanical systems or MEMS), piezoelectric micromachined ultrasonic transducers (PMUT, based on miniaturized flexural piezoelectric films), optoacoustic transducers (based on the photoacoustic effect), electrodynamic transducers (based on Faraday's induction law), or electrohydraulic transducers (based on a fast bubble cavitation generated by a spark plug immersed in water). Covering all these ultrasound generation techniques in detail is beyond the scope of this chapter. Here, we will focus on piezoelectric transducers, as they are the most common transducers for medical applications.

3.2 Piezoelectricity

Piezoelectric materials are the most common in medical ultrasound transducers, most ultrasound imaging probes and modern therapeutic ultrasound devices are based on this technology. Piezoelectricity, discovered by the brothers Pierre and Jacques Curie in 1880 [1], is the property of several materials to accumulate electrical charge when the medium is deformed, and, conversely, to deform under the action of an external electric field. The piezoelectric effect occurs in solids with a nonsymmetrical crystalline structure. When the asymmetric crystalline structure is deformed under external stress, a polarization occurs, as seen in Figure 3.1. This causes a flow of electrons to accumulate at one end of the crystal until electrostatic equilibrium is reached [2]. In this way, an electric field appears inside the piezoelectric when it is deformed. It should be noted that the piezoelectric effect also occurs in the reverse direction, i.e. a piezoelectric crystal subjected to an electric potential difference will deform until electrostatic equilibrium is reached inside the crystal. Thus, piezoelectric materials are used both as sensors/receivers (direct piezoelectric effect) and actuators/emitters (reverse piezoelectric effect).

3.2.1 Model Equations

The complete modeling of piezoelectric material dynamics is a complex problem, mainly due to the tensor character of the stresses together with the material anisotropy, both in the elastic and piezoelectric properties, of piezoelectric solids. In addition, the materials exhibit viscoelastic behavior and other phenomena such as nonlinearity, hysteresis or dependence of elasticity and piezoelectricity

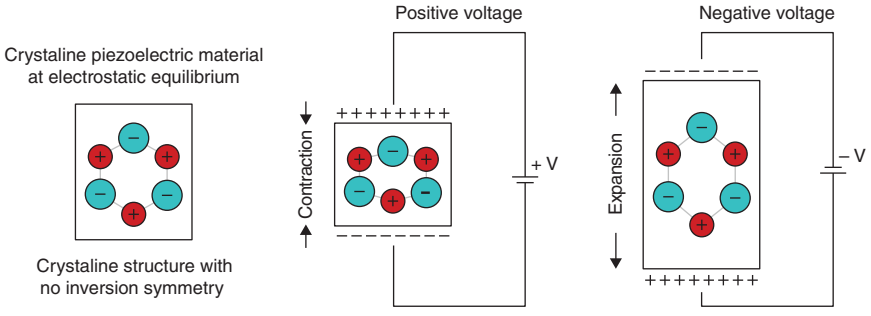


Figure 3.1 Piezoelectric effect in a crystal with non-inversion symmetry. When the material is at electrostatic equilibrium the centers of positive and negative charges are not at the same position. When the material is compressed the crystal structure is deformed and due to asymmetric charge distribution an electrical potential is observed. On the other hand, when the crystal is expanded the opposite effect is observed and a negative electric potential is generated. The inverse piezoelectric effect also appears: the material deforms when an electrical potential is imposed to maintain electrostatic equilibrium.

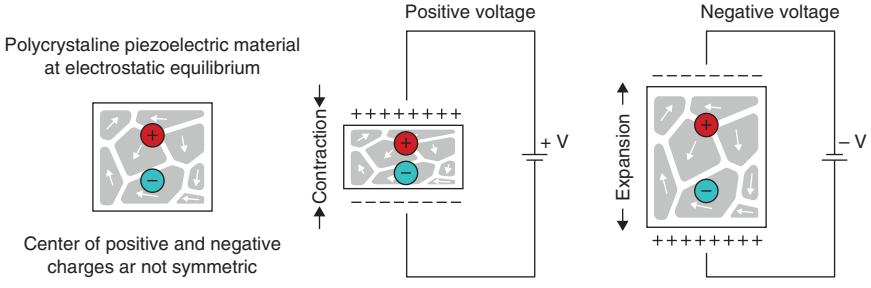


Figure 3.2 Piezoelectric effect in a polycrystaline material. When the material is at electrostatic equilibrium the centers of positive and negative charges are not in the same position. When the material is compressed the polycrystaline structure is deformed and due to asymmetric charge distribution an electrical potential is observed. On the other hand, when the polycrystaline is expanded the opposite effect is observed and a negative electric potential is generated. The inverse piezoelectric effect also appears: the material deforms when an electrical potential is imposed to maintain electrostatic equilibrium.

on temperature. However, there are simplified configurations that allow their description by means of simple models, such as the vibration of a piezoelectric ceramic in thickness model. Indeed, this case is of particular interest in engineering since the coupling with the surrounding medium is very efficient: the deformations produced by the piezoelectric can be transmitted to another medium in the form of acoustic or longitudinal elastic waves, e.g. as those used for ultrasound imaging (Figure 3.2).

3.2.1.1 Stress-Charge Formulation

In the piezoelectric material the ratio between the stress tensor, $\boldsymbol{T}$ (N/m^2), the strain tensor, $\boldsymbol{S}$ (dimensionless), the electric field vector, $\boldsymbol{E}$ (V/m) and electric displacement vector, $\boldsymbol{D}$ (C/m^2), are given by the piezoelectric constitutive equations [3]

$$\boldsymbol{T} = \boldsymbol{c}^E\mathbf{S} - \mathbf{e}^t\boldsymbol{E} \tag{3.1}$$

$$\boldsymbol{D} = \boldsymbol{\varepsilon}^S \boldsymbol{E} + \mathbf{e}\boldsymbol{S} \tag{3.2}$$

where $\boldsymbol{c}^E$ (N/m^2) is the matrix of elastic moduli for constant electric field and $\boldsymbol{\varepsilon}^S$ (F/m) is the permittivity matrix of the material for constant strain. In general, the superscript indicates the magnitude that remains invariant when a constant is defined. Finally, $\mathbf{e}$ (C/m^2) is the piezoelectric constant matrix, being $\mathbf{e}^t$ its respective transposed matrix. In the system (3.1)–(3.2), the first terms on the right-hand side represent the elastic and electrical behavior of the material, while the second terms represent the coupling between the two quantities, i.e. the piezoelectricity.

3.2.1.2 Strain-Charge Formulation

The constitutive piezoelectric Eqs. (3.1)–(3.2) in stress-charge formulation can be formulated strain-charge formulation, resulting in the governing equations

$$\boldsymbol{S} = \boldsymbol{s}^E \boldsymbol{T} + \boldsymbol{d}\mathbf{E} \tag{3.3}$$

$$\boldsymbol{D} = \boldsymbol{\varepsilon}^T \boldsymbol{E} + \boldsymbol{d}^t \boldsymbol{T} \tag{3.4}$$

where $\boldsymbol{s}^E$ (N/m^2) is the elastic compliance matrix for constant electric field and $\boldsymbol{\varepsilon}^T$ (F/m) is the permittivity matrix of the material for constant stress. Finally, $\boldsymbol{d}$ (C/N) is the piezoelectric constant matrix, being $\boldsymbol{d}^t$ its respective transposed matrix.

3.2.1.3 Stress-Field Formulation

In an analogous way, we can also derive piezoelectric constitutive equations for a stress-field formulation. In this way, the system can be written as

$$\boldsymbol{T} = \boldsymbol{c}^D \boldsymbol{S} - \boldsymbol{h}^t \boldsymbol{D} \tag{3.5}$$

$$\boldsymbol{E} = \boldsymbol{\beta}^S \boldsymbol{D} - \boldsymbol{h}\boldsymbol{S} \tag{3.6}$$

where $\boldsymbol{\beta}^S$ is the inverse permittivity at constant strain, and $\boldsymbol{h}$ is the piezoelectric constant matrix for the stress-field formulation.

3.2.1.4 Strain-Field Formulation

Finally, in a strain-field formulation, the piezoelectric equations are

$$\boldsymbol{S} = \boldsymbol{s}^D \boldsymbol{T} + \boldsymbol{g}^t \boldsymbol{D} \tag{3.7}$$

$$\boldsymbol{E} = \boldsymbol{\beta}^T \boldsymbol{D} - \boldsymbol{g}\boldsymbol{T} \tag{3.8}$$

where $\boldsymbol{\beta}^T$ is the inverse permittivity at constant stress, and $\boldsymbol{g}$ (Vm/N) is the piezoelectric constant matrix for the strain-field formulation.

3.2.2 The Piezoelectric Constants

Writing the system in either way is interesting to design specific sensors or actuators, and one should keep in mind that piezoelectric material manufacturers and laboratories indifferently measure one or the other in the characterization of the piezoelectric constants. It is worth remembering that

$$\mathbf{c}^E = \frac{1}{\mathbf{s}^E}, \quad \mathbf{c}^D = \frac{1}{\mathbf{s}^D} \quad \boldsymbol{\varepsilon}^S = \frac{1}{\boldsymbol{\beta}^S}, \quad \boldsymbol{\varepsilon}^D = \frac{1}{\boldsymbol{\beta}^D} \tag{3.9}$$

but on the other hand

$$\mathbf{c}^E \neq \mathbf{c}^D, \quad \mathbf{s}^E \neq \mathbf{s}^D \quad \boldsymbol{\varepsilon}^S \neq \boldsymbol{\varepsilon}^T, \quad \boldsymbol{\beta}^S \neq \boldsymbol{\beta}^T \tag{3.10}$$

Therefore, special care must be taken when choosing one set of elastic and electrical constants. In three spatial dimensions, the system of constitutive Eqs. (3.1–3.2) for a piezoelectric material can be written as

$$\begin{bmatrix} S_1 \\ S_2 \\ S_3 \\ S_4 \\ S_5 \\ S_6 \\ D_1 \\ D_2 \\ D_3 \end{bmatrix} = \begin{bmatrix} s_{11}^E & s_{12}^E & s_{13}^E & s_{14}^E & s_{15}^E & s_{16}^E & d_{11} & d_{12} & d_{13} \\ s_{21}^E & s_{22}^E & s_{23}^E & s_{24}^E & s_{25}^E & s_{26}^E & d_{21} & d_{22} & d_{23} \\ s_{31}^E & s_{32}^E & s_{33}^E & s_{34}^E & s_{35}^E & s_{36}^E & d_{31} & d_{32} & d_{33} \\ s_{41}^E & s_{42}^E & s_{43}^E & s_{44}^E & s_{45}^E & s_{46}^E & d_{41} & d_{42} & d_{43} \\ s_{51}^E & s_{52}^E & s_{53}^E & s_{54}^E & s_{55}^E & s_{56}^E & d_{51} & d_{52} & d_{53} \\ s_{61}^E & s_{62}^E & s_{63}^E & s_{64}^E & s_{65}^E & s_{66}^E & d_{61} & d_{62} & d_{63} \\ d_{11} & d_{12} & d_{63} & d_{14} & d_{15} & d_{16} & \varepsilon_{11}^T & \varepsilon_{12}^T & \varepsilon_{13}^T \\ d_{21} & d_{22} & d_{63} & d_{24} & d_{25} & d_{26} & \varepsilon_{21}^T & \varepsilon_{22}^T & \varepsilon_{23}^T \\ d_{31} & d_{32} & d_{63} & d_{34} & d_{35} & d_{36} & \varepsilon_{31}^T & \varepsilon_{32}^T & \varepsilon_{33}^T \end{bmatrix} \begin{bmatrix} T_1 \\ T_2 \\ T_3 \\ T_4 \\ T_5 \\ T_6 \\ E_1 \\ E_2 \\ E_3 \end{bmatrix} \tag{3.11}$$

where we introduced the Voigt notation convention for the components $1 = xx$, $2 = yy$, $3 = zz$, $4 = xy$, $5 = yz$, and $6 = zx$. However, to analyze an ultrasonic transducer, this general set of equations can be simplified because most of the piezoelectric constants are negligible (or zero) due to the specific crystalline structure of the material and poling direction.

3.2.3 Longitudinal Motion in a Piezoelectric Material

Generally, in piezoelectric materials, such as quartz or lead zirconate titanate (PZT), many of the piezoelectric constants are zero (or negligible) due to the symmetry of the crystal, i.e. the piezoelectric effect only occurs efficiently in some particular directions.

3.2.3.1 A Simple Piezoelectric Model

For the present example, we will consider vibrations that occur only in thickness, ignoring what happens in other directions by reducing the system of equations to variations in the x_3 direction, as shown in Figure 3.3. This models the thickness motion of a slab, for example a disc, of piezoelectric material with two electrodes on its faces, polling direction x_3, and a high piezoelectric constant h_33. Thus, the system of equations given by (3.5) and (3.6) is reduced to

$$T_3 = c_{33}^D S_{33} - h_{33} D_3 \tag{3.12}$$

$$E_3 = \beta_{33}^S D_3 - h_{33} S_3 \tag{3.13}$$

These equations describe the system in the x_3 direction assuming that the other piezoelectric and elastic moduli are zero (which is not the case in a real ceramic).

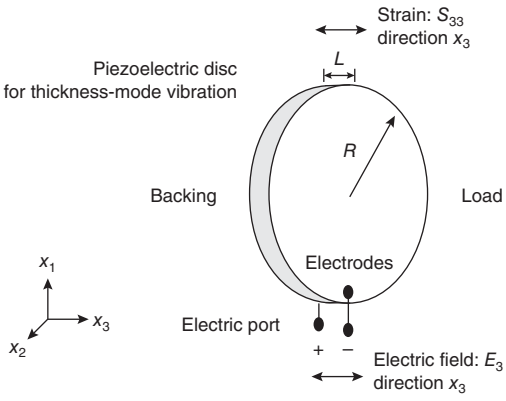


Figure 3.3 Piezoelectric disc for vibration in thickness mode.

3.2.3.2 Waves in the Piezoelectric Material

To close the system, we can use Newton's Second Law to make a balance of forces

$$\rho_p \frac{\partial^2 \xi_3}{\partial t^2} = \frac{\partial T_3}{\partial x_3} \tag{3.14}$$

where ρ_p is the density in the piezoelectric material and ξ_3 is the displacement of the material relative to its equilibrium position in the direction x_3. In this equation the first term expresses the product of the mass and the acceleration of the system, and the second the force produced by the stress field. The deformation is defined as a function of the displacement, ξ_3, as

$$S_{33} = \frac{\partial \xi_3}{\partial x_3} \tag{3.15}$$

and the particle velocity as

$$v_3 = \frac{\partial \xi_3}{\partial t} \tag{3.16}$$

Thus, the deformation is related to the particle velocity as

$$\frac{\partial S_{33}}{\partial t} = \frac{\partial}{\partial t}\left(\frac{\partial \xi_3}{\partial x_3}\right) = \frac{\partial}{\partial x_3}\left(\frac{\partial \xi_3}{\partial t}\right) = \frac{\partial v_3}{\partial x_3} \tag{3.17}$$

Finally, we differentiate with respect to time the constitutive equations to obtain

$$\rho_p \frac{\partial v_3}{\partial t} = \frac{\partial T_3}{\partial x_3}, \tag{3.18}$$

$$\frac{\partial T_3}{\partial t} = c_{33}^D \frac{\partial v_3}{\partial x_3} - h_{33} \frac{\partial D_3}{\partial t}, \tag{3.19}$$

$$\frac{\partial E_3}{\partial t} = \beta_{33}^S \frac{\partial D_3}{\partial t} - h_{33} \frac{\partial v_3}{\partial x_3} \tag{3.20}$$

These equations describe the dynamics of the system in the x_3 direction. Equations (3.18) and (3.19) are equivalent to the constitutive relations of acoustics for

longitudinal motion in one dimension. For example, in open circuit these can be combined into a wave equation where the sound speed is

$$c_p = \sqrt{\frac{c_{33}^D}{\rho_p}} \tag{3.21}$$

Like any other solid material, piezoelectric media transmit waves. The main difference with the acoustic equations is the coupling with the partial differential equation (PDE) electric equation through the piezoelectric constant h_{33}. The coupling implies that variations on the electric field will induce particle velocity gradients and, therefore strain, and these perturbations will propagate as a longitudinal motion through the material. Equations (3.18) and (3.19) can be solved directly by applying numerical or analytical methods when the boundary conditions are known. For example, Richard Krimholtz et al., proposed in 1970 a model commonly referred to as the Krimholtz, Leedom, and Matthaei model (KLM) equivalent circuit [4] to describe the motion of a piezoelectric layer in the frequency domain. This kind of model allows a great flexibility to add additional elements to the transducer, such as backing layers, impedance matching layers, and electronic components, as we will show below.

3.3 Piezoelectric Materials

There exist several types of materials that exhibit piezoelectricity. These include crystals, piezoelectric ceramics, piezoelectric polymers, and piezoelectric composites. However, in all these materials, piezoelectricity is only observed at low temperatures, when nonsymmetric microscopic crystalline structure holds under deformation. Above a critical temperature, called the Curie temperature, T_C, ferroelectric materials undergo a phase transition, shifting from a low-temperature ferroelectric phase to a high-temperature paraelectric phase [5]. Therefore, above T_C both ferroelectricity and piezoelectricity disappear and the material vibrates as common (visco)elastic solid. Therefore, for practical applications a higher Curie temperature is recommended to achieve better stability and operational range.

The electromechanical coupling factors, k_{ij}, are usually used to measure the performance of a piezoelectric material. They quantify the conversion of mechanical to electrical energy. Common electromechanical coupling factors provided by manufactures are defined as

$$k_{33} = \frac{d_{33}}{\sqrt{S_{33}\epsilon_{33}}} \quad k_{31} = \frac{d_{31}}{\sqrt{S_{11}\epsilon_{33}}} \quad k_{15} = \frac{d_{15}}{\sqrt{S_{44}\epsilon_{11}}} \tag{3.22}$$

where, following a Voigt notation, subscripts 4 and 5 refer to planes normal to the 1 and 2 axis, respectively. Therefore, they indicate how efficiently the material deforms in a given direction under the action of an electric field in other direction. Note these quantities are dimensionless.

3.3.1 Piezoelectric Crystals

Piezoelectric crystals can be found in nature, for example, quartz (SiO_2), berlinite, sucrose, Rochelle salt ($NaKC_4H_4O_64H_2O$), topaz, and a tourmaline group of

minerals. However, natural crystals present weak piezoelectric properties as compared with synthetic materials, e.g. piezoelectric ceramics, as we will see below. Crystalline structures can also be synthesized in the laboratory to obtain piezoelectric substances such as gallium orthophosphate ($GaPO_4$) and langasite ($La_3Ga_5SiO_{14}$).

3.3.2 Piezoelectric Ceramics

Piezoelectric ceramics are substances largely used in industry because it can be synthesized with great flexibility and at relatively low cost [6]. These include most of the standard piezoelectric as the common lead zirconate titanate ($Pb[Zr_x\ Ti_{1-x}]O_3$), known as PZT. The basic composition of PZT is doped with several elements to achieve different properties, which are usually proprietary formulas of manufactures. For example, PZT-4 is doped with Fe, PZT-5 with Nb-doping, PZT-6 with Cr-doping, or PZT-7 with La-doping. Some commonly used compositions include lead titanate ($PbTiO_3$), potassium niobate ($KNbO_3$), zinc oxide (ZnO), or sodium tungstate ($NaWO_3$). Piezoelectric ceramics such as PZT are very efficient materials showing a high electromechanical coupling factor. They also show a high stiffness and high dielectric constant, while they present low elastic and dielectric losses [7].

However, the lead content of most piezoceramics, harmful for living organisms during usage, manufacturing and disposal, have risen the attention to use lead-free synthetic piezoceramics [8], such as long time known barium titanate ($BaTiO_3$), and to design more efficient materials such as lithium niobate ($LiNbO_3$), lithium tantalate ($LiTaO_3$), aluminium nitride (AlN), scandium–aluminum nitride, sodium niobate ($NaNbO_3$) or bismuth ferrite ($BiFeO_3$), etc [9]. However, manufacturing some of these materials can result in a large environmental impact due to mining and processing.

3.3.3 Piezoelectric Polymers

Polymerization can be used to obtain piezoelectric substances such as polyvinylidene fluoride (PVDF) films and copolymers of vinylidene fluoride (VDF) with trifluoroethylene (TrFE), or with tetrafluroethylene (TeFE) [10]. Piezopolymers present desirable mechanical and functional properties such as flexibility, durability and biocompatibility, and low-cost manufacturing, while they feature a low dielectric constant and a low acoustic impedance, which provides an excellent matching with water or tissues [11]. However, they are less efficient than piezoceramics and because they are currently manufactured in thin films, their practical use for actuators is limited, and they are mostly used for sensors.

3.3.4 Piezoelectric Composites

Finally, piezocomposites can also be manufactured by mixing two phases, usually a stiff piezoceramic matrix filled by a soft polymer [12]. Piezoelectric composites are efficient, presenting a good electromechanical coupling factor. In addition, they avoid the mechanical fragility of piezoceramics. These materials also present a low

acoustic impedance improving the impedance matching with water. Composites are manufactured in several ways, the active phase can be made of piezoceramic rods or fibers, blended by a viscoelastic resin, molded in bulky shapes or thin films. Piezoelectric coating has been proposed by polling a mix of PTZ powder and epoxy resin.

3.4 Ultrasound Transducers

The piezoelectric material is the main element of the transducer, as it transforms electric fields into elastic waves and vice versa. However, it is important to note that, in practice, the piezoelectric element will never vibrate uncoupled from surrounding materials. Transducers are usually composed of more elements.

3.4.1 Elements of a Transducer

In a real transducer we usually have, at least, a load on both sides of the piezoelectric element: the radiation load and backing layer, respectively. Commonly more elastic layers are located between the load and the piezoelectric element to enhance the transmission of acoustic energy. In addition, the electrical port is connected to some electrical network, the signal generator and amplifier, connection wires, etc. The complete set of mechanical and electrical elements that allow us to use the piezoelectric effect to emit or to detect acoustic waves is called a transducer. A basic example for a longitudinal transducer, where the piezoelectric vibrates in thickness mode, is the one shown in Figure 3.4.

3.4.2 The Piezoelectric Slab

The slab of piezoelectric material is the main element of the transducer. As in any vibrating solid, the geometry of the material and its properties govern its dynamics.

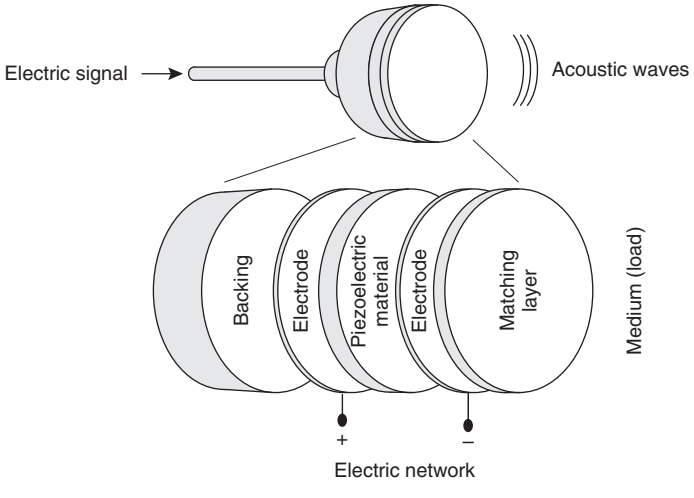


Figure 3.4 Model of a basic ultrasound piezoelectric transducer for vibration in thickness mode.

For example, a disc of piezoelectric material exhibit longitudinal resonance modes. For the thickness mode, as described before, the longitudinal modes of a piezoelectric slab of thickness L appear when $L = n\lambda/2$, where λ is the wavelength in the piezoelectric material, and $n = 1,3,5, \ldots$, i.e. at odd multiplies of the first longitudinal resonance frequency. Note that a disc will also show radial modes, that can appear at lower frequencies, but typically the coupling strength is larger for the first axial mode ($L = \lambda/2$). In addition, this mode is efficiently coupled with longitudinal waves in fluids or tissues, because the piezoelectric produces a uniform axial deformation along the disc surface, compressing the fluid and generating acoustic waves. However, note that eigenmodes also depend on boundary conditions, i.e. the surrounding material impedance and its geometry, the clamping strength on the piezoelectric boundaries, but also the electric impedance on its electrodes.

3.4.3 Matching Layers

On the front side of the ceramic is a layer of elastic solid material called an impedance matching layer. The function of this layer is to improve the energy transfer from the piezoelectric layer to the medium to be radiated. This is necessary because of the large difference in acoustic impedance between the piezoelectric material and the radiation load, in many cases water or tissue for biomedical applications. While this layer is mandatory in piezoceramics and piezoelectric crystals designs, while it can be neglected when using soft piezoelectric polymers.

3.4.3.1 Classical Matching Layer Design

The design of matching layers considers that the transmission coefficient of acoustic energy between a layer of material located between the piezoelectric material and the radiation medium should be the maximum at a design frequency. In theory, the transmission can reach the unity when two conditions are fulfilled. The first condition is that the impedance of the matching material should be the geometric mean of the load and the piezoelectric medium, as [9]

$$Z_m = \sqrt{Z_p Z_L} \tag{3.23}$$

where $Z_m = \rho_m c_m$, $Z_p = \rho_p c_p$, and $Z_L = \rho_L c_L$ are the impedance of the matching layer, the piezoelectric material, and the load; and c_m, c_p, and c_L; and ρ_m, ρ_p, and ρ_L are their sound speed and mass density, respectively. For biomedical ultrasound transducers, typical acoustic impedance for piezoceramics is about 15–30 MRayl, tissue or water impedance is about 1.5 MRayl, so the material of the layer should be tuned to have specific impedance values, about 3–15 MRayl. This is achieved using epoxy, polyurethane or polystyrene layers, that can be doped with metal powder to increase its density. The second condition is that the length of the layer, L_m, should be one quarter of the wavelength in the matching material

$$L_m = \frac{\lambda_m}{4} \tag{3.24}$$

where $\lambda_m = c_m/f_0$ is the wavelength in the matching layer material at the design frequency f_0. This last equation implies that transmission will only be the unity at

one specific frequency. For therapeutic ultrasound transducers and actuators this can be of interest because they are typically designed for narrow frequency range. For example, therapeutic ultrasound transducers for high-intensity focused ultrasound radiate long sinusoidal bursts, with thousands of cycles at frequencies around 1 MHz, i.e. a narrow matching bandwidth is enough. However, for imaging a short pulse of about one cycle is needed for a good axial resolution, therefore, a large bandwidth is required.

3.4.3.2 Multiple Matching Layer Design

A solution to increase the bandwidth is to include several matching layers, typically two or three. This creates an impedance gradient and acoustic energy can smoothly penetrate for detection into the transducer (or radiate for emission) [13]. If one consider a total of N layers, the material of each layer can be chosen to fulfill the following condition [14]

$$Z_n = \sqrt[N+1]{Z_p^{(N-n+1)} Z_L^n} \tag{3.25}$$

where $Z_n = \rho_n c_n$ is the impedance, ρ_n the density, and c_n the sound speed of the nth layer. Note that for $N = 1$, this equation collapse to (3.23). The length of the nth matching layer is given by

$$L_n = \frac{\lambda_n}{4} \tag{3.26}$$

where $\lambda_n = c_n/f_0$ is the wavelength in the nth matching layer. One should keep in mind that perfect transmission is never achieved due to viscoelastic losses, the more layers are added, the more important the losses are, limiting the total thickness of the set of impedance matching layers. For example, ultrasound imaging transducers usually are manufactures with one or two matching layers.

3.4.3.3 Broadband Matching Layer Design

Other designs include the electromechanical coupling and the broadband considerations, resulting in a modified impedance matching condition of Eq. (3.23) as [15]

$$Z_m = Z_p^{1/3} Z_L^{2/3} \tag{3.27}$$

for a matching single-layer design. For double matching layer we can use [16]

$$Z_{m1} = Z_p^{4/7} Z_L^{3/7}, \quad \text{and} \quad Z_{m2} = Z_p^{1/7} Z_L^{6/7} \tag{3.28}$$

to improve the bandwidth of the transmitted spectrum.

3.4.4 Backing Layer

Another element of the transducer is the backing layer or simply known as *backing*. By adjusting the properties of this layer we can design transducers with a long temporal response and narrow bandwidth or, conversely, with a short impulse response and wide bandwidth [17]. When the impedance difference between the piezoelectric element and the backing is very high, the energy is almost entirely reflected at

the rear interface, maximizing the radiation toward the front face. For example, if a very low impedance backing is present, such as air, the quality factor of the resonance of the piezoelectric transducer is high, and its bandwidth is very narrow. This is desirable in actuators such as therapeutic ultrasound transducers.

However, for imaging, a broad frequency range is needed for axial resolution. To damp the resonance of the piezoelectric slab, the backing material should be absorbent and impedance matched with the piezoelectric. In imaging transducers the impedance difference between the active element and the backing is usually small and damping is introduced into the backing material through viscoelastic losses and doping. In this way, the resonance of the transducer is damped and a broad bandwidth response is obtained. However, increasing the operating frequency range in this way leads to a loss of efficiency because part of the energy is not radiated. In addition, absorbing backing materials can heat up under high-intensity ultrasound, therefore, attention should be paid when using long and high voltage pulsed burst signals for imaging transducers such as pulse-coded excitation techniques or elastography.

Materials to design backing layers include conductive epoxy, whose impedance is about 6 MRayl and large attenuation coefficients (120 dB/mm at 30 MHz), or doped epoxy such as tungsten-loaded epoxy to increase its impedance up to 8–20 MRayl, between others.

3.4.5 Electrical Impedance Matching Network

Finally, it is common for the ultrasonic transducer to require an electrical impedance matching network to optimize the energy transfer through the electrical port. This network couples the electrical impedance between the excitation/detection system and the piezoelectric element. For narrow bandwidth systems, this network can be built using a few passive electronic components. However, the complexity of the network increases for broadband ultrasound transducers as those used for imaging.

3.5 Ultrasound Beams

Once the ultrasound transducer vibrates in thickness mode, the vibrating surface generates an acoustic beam that propagates, usually, through water or soft tissue. The specific features of ultrasound beam mainly depend on the source size and frequency and its geometry.

3.5.1 Circular Aperture Transducers

One simple but common case of transducer is the case of a flat circular source vibrating in thickness mode. In this case, we can consider a flat circular surface of radius a, which moves uniformly with velocity $v_0 \exp(i\omega t)$ normal to its surface, and which is fixed on a rigid infinite panel, called a baffle, where the velocity is zero.[1] To obtain the

1 The baffle is introduced to simplify the analysis, similar results are obtained without considering this boundary condition.

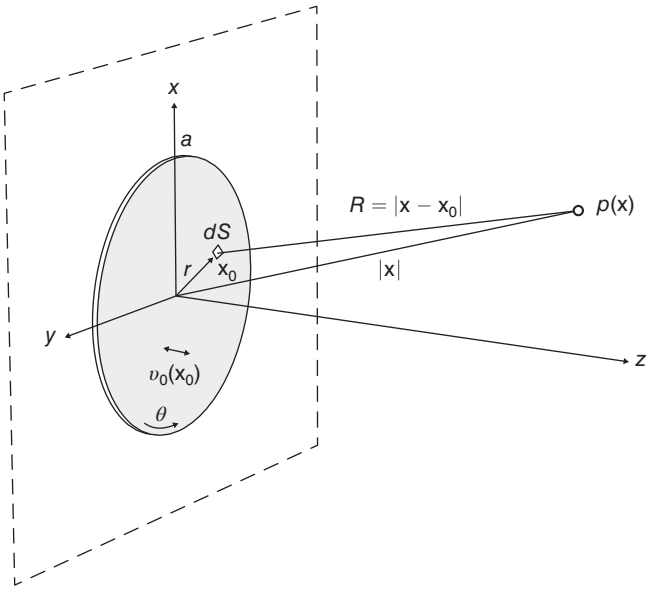


Figure 3.5 Diagram of a flat circular transducer and calculation points.

acoustic field, we will divide the circular surface into infinitesimal surface elements dS, each of which will act as a single source. Thus, using the Rayleigh–Sommerfeld integral, the acoustic field at any point is given by

$$p(\mathbf{x}, t) = \frac{i\omega\rho_0 v_0}{2\pi}\int_S \frac{e^{i(\omega t - kR)}}{R} dS \tag{3.29}$$

Although this integral is difficult to solve in general, we can find a general solution for the acoustic field in series form [18, 19]. Although the complete solution is valid at any point in space, the series converges slowly and the solution is not compact (Figure 3.5). However, if we restrict the validity only along the axis of the transducer, we can have the compact analytical solution along the z coordinate and on the symmetry axis, when $x = 0$ and $y = 0$, and therefore $r = 0$ and $\theta = 0$. In this case, $R = \sqrt{r_0^2 + z^2}$, leading to

$$p(z, t) = p_0 \left[e^{i(\omega t - kz)} - e^{i(\omega t - k\sqrt{a^2+z^2})} \right] \tag{3.30}$$

where $p_0 = c_0\rho_0 v_0$. The solution on the acoustic axis is built by the superposition of two waves, a plane wave, given by the term $\exp(-ikz)$, and a wave traveling from the edge of the piston, given by the term $\exp(-ik\sqrt{a^2 + z^2})$. The plane wave describes the radiation from the flat piston, while the second wave introduces diffraction effects at the piston edge. Taking the absolute value of Eq. (3.30) we obtain the amplitude of the field along the axis

$$|p(z, t)| = 2p_0 \left| \sin\left(\frac{1}{2} kz \left[\sqrt{1 + \frac{a^2}{z^2}} - 1 \right] \right) \right| \tag{3.31}$$

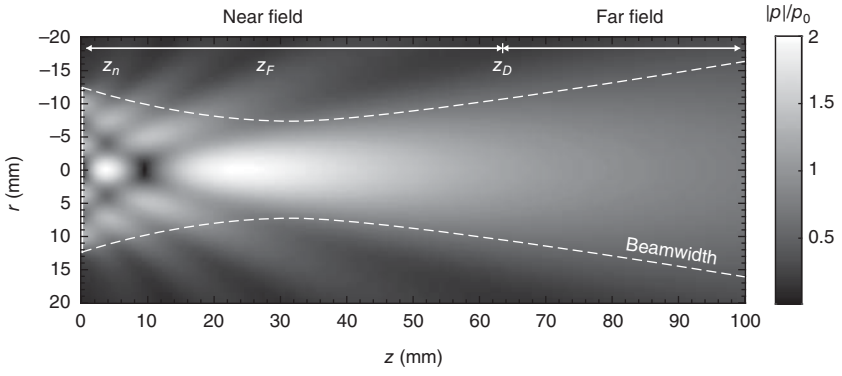


Figure 3.6 Example of the field radiated by a circular piston of aperture $2a = 25$ mm and frequency 244 kHz.

Near the surface, these waves interfere constructively and destructively and oscillations are present, therefore the pressure varies between 0 and $2p_0$ (Figure 3.6).

The maxima in the radiation field of a flat piston will occur at the distances from the axis that satisfy

$$z_n = \frac{(ka)^2 - (n\pi)^2}{2\pi kn} \tag{3.32}$$

where $n = 1,3,5,\ldots$. The oscillating area near the piston is known as the Fresnel region. This function has an ultimate maximum, which appears at a distance from the transducer of $z_1 = ka^2/2\pi - \pi/2k$. Since $ka^2/2\pi \gg \pi/2k$ in most acoustic problems, the Fresnel distance is defined as the distance at which the last maximum approximately appears

$$z_F = \frac{ka^2}{2\pi} \tag{3.33}$$

From the latter maximum, the field starts to decrease progressively. The diffraction distance, also known as Rayleigh distance, is given by

$$z_D = \frac{ka^2}{2} \tag{3.34}$$

and defines the point from which the field amplitude begins to decay inversely with distance at a rate of $1/z$. This length marks the transition between the near field and the far field. It is worth noting there that transducers with other geometries such as rectangular radiating surfaces show a roughly similar pattern, an oscillating near field, and beyond the Rayleigh distance the field decays with the inverse of the distance.

3.5.2 Focused Transducers

For certain applications, surfaces with curved geometry are also used, so that, due to the curvature, acoustic waves converge toward a given point and the energy is

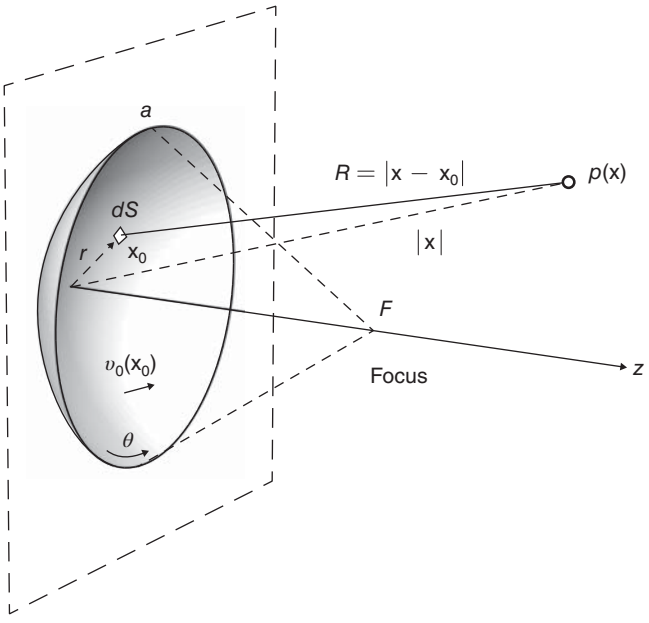


Figure 3.7 Schematic of a focused acoustic transducer and calculation points.

concentrated on a focal zone. In the case of the spherical cap of radius of curvature F and aperture radius a, as shown in Figure 3.7, we can also find analytical solutions of Eq. (3.29), such as those obtained on the symmetry axis by [20], or for the whole field but in paraxial approximation by [21] or [22].

A complete solution for the amplitude of the on-axis field is given by

$$p(z,\omega) \approx 2p_0 \left| \frac{1}{1-\tilde{z}} \sin\left(k \frac{z - R_{max}}{2} \right) \right| \tag{3.35}$$

where F is the radius of curvature of the piston, $\tilde{z} = z/F$, a is the average aperture and R_{max} is calculated as

$$R_{max} = F\sqrt{1 + (1-\tilde{z})^2 - 2(1-\tilde{z})\sqrt{1 - \frac{a^2}{F^2}}} \tag{3.36}$$

This solution is valid for all apertures, but for moderately focused surfaces, when $F \gg a$, using a paraxial approximation of the diffraction we obtain

$$p(z,\omega) \approx 2p_0 \left| \frac{1}{1-\tilde{z}} \sin\left(G \frac{1-\tilde{z}}{2\tilde{z}} \right) \right| \tag{3.37}$$

where $G = z_D/F = ka^2/2F$ is the transducer gain, which measures the increase in sound pressure at the geometric focus relative to the pressure at the source surface.

As in the case of the circular surface, we can also distinguish between near-field and far-field zones. Within the near field we find three distinct regions. Near the piston, for $z < z_N$, the near Fresnel zone extends, where there are strong oscillations

due to constructive and destructive interference. We define the Fresnel distance in this case as

$$z_N = \frac{F}{1 + F\lambda/a^2} \tag{3.38}$$

The Fraunhofer zone comprises the acoustic focus and the geometric focus of the source. In this region, the beamwidth is minimal, and the acoustic energy is highly concentrated. It is important to note that the acoustic focus, i.e. the area of maximum energy, does not generally coincide with the geometric focus due to diffraction effects. If there are no nonlinear effects and the medium is homogeneous, the acoustic focus appears closer to the transducer than the geometric focus. Beyond the Fraunhofer zone, $z > z_F$, where

$$z_F = \frac{F}{1 - F\lambda/a^2} \tag{3.39}$$

extends the far Fresnel zone, in which there are also oscillations, but they are softer and of smaller amplitude. Progressively, they disappear.

Figure 3.8 shows a schematic of these near-field regions. An important parameter to characterizing a focused transducer is its gain, G, defined as the field amplitude at the geometric focus, $z = F$, compared with the field at the surface of the source, given by

$$G = \left|\frac{p_F}{p_0}\right| = p_0 \frac{ka^2}{2F} \tag{3.40}$$

It is critical to note that since the maximum amplitude value of the field occurs before the geometric focus, the maximum amplitude at the acoustic focus is somewhat larger than p_F. The point at which, in a paraxial approximation, a maximum occurs in the field given by Eq. (3.37), is given by [23]

$$z_{max} = F\frac{3G}{2G + \sqrt{G^2 + 72}} \tag{3.41}$$

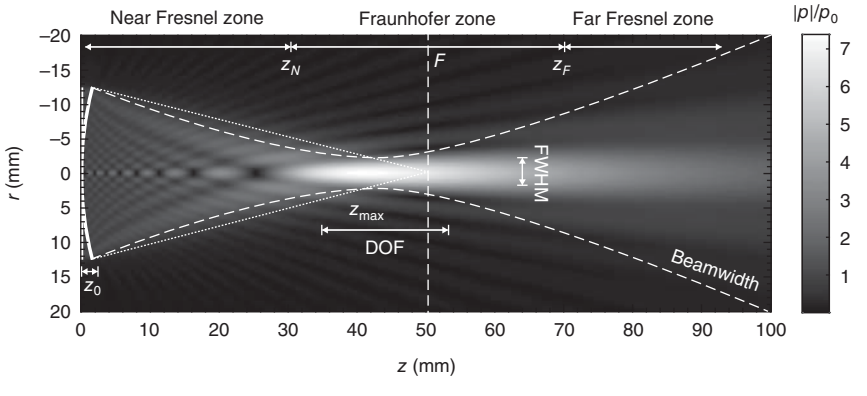


Figure 3.8 Example of the field produced by an aperture focused transducer $2a = 25$ mm, frequency 1 MHz, and focal $F = 50$ mm.

Note that the position of the acoustic focus depends on the initial amplitude [24, 25], but if the vibration amplitude is small we can consider linear propagation and, therefore, this effect is negligible.

On the other hand, it is relevant to characterize the focus in terms of its lateral and axial width (or depth of field), defined at half the maximum pressure in the acoustic focus

$$FWHM = 0.7\frac{F\lambda}{a} \tag{3.42}$$

for the transverse width, and

$$DOF = 1.8\frac{F^2\lambda}{a^2} \tag{3.43}$$

for the depth of field in the axial direction. Other points of interest are the exit plane, the distance of which is given by $z = F - \sqrt{F^2 - a^2}$, or the coverage angle, given by $\beta = \arcsin a/F$.

3.5.3 Phased-Array Transducers

For many applications transducers are composed of many small piezoelectric elements. In these transducers each active element is excited with an individual electric signal, and in analogy with phased-array antennas for electromagnetic RADAR systems, they are named phased-array transducers. These transducers are used for SONAR systems in underwater acoustics, and are also very common in biomedical applications for ultrasound imaging. Phased-array transducers can be manufactured in several configurations such as linear arrays, convex probes, sectorial arrays, two-dimensional (2D) transducer arrays, or small endocavitary ultrasound transducer to perform internal examinations such as endovaginal or endorectal probes. An example of a linear phased-array probe is shown in Figure 3.9.

By setting individual delays for each excitation signal, the transducer can modulate the transmitted wavefront to transmit focusing beams and control the location of the focus, e.g. in a linear array we can control its depth and lateral position. In addition, phased-array transducers offer a great flexibility to conform other wavefronts, such as steered quasi-plane wavefronts as those used for plane-wave compounding imaging or even spherically diverging beams. In many imaging modalities a partial aperture is used for each transmission, and usually this is controlled by using channel apodization. This consists on setting a spatial window to the channel amplitude, usually a Gaussian function, to reduce lateral lobes.

3.6 Acoustic Lenses

As we have presented previously, beam shaping and focusing can be obtained by curved radiating surfaces, for example, using spherically shaped piezoelectric ceramics. However, in most cases using a curved piezoelectric transducer increases the cost and the complexity of the transducer. In addition, the coupling with tissues

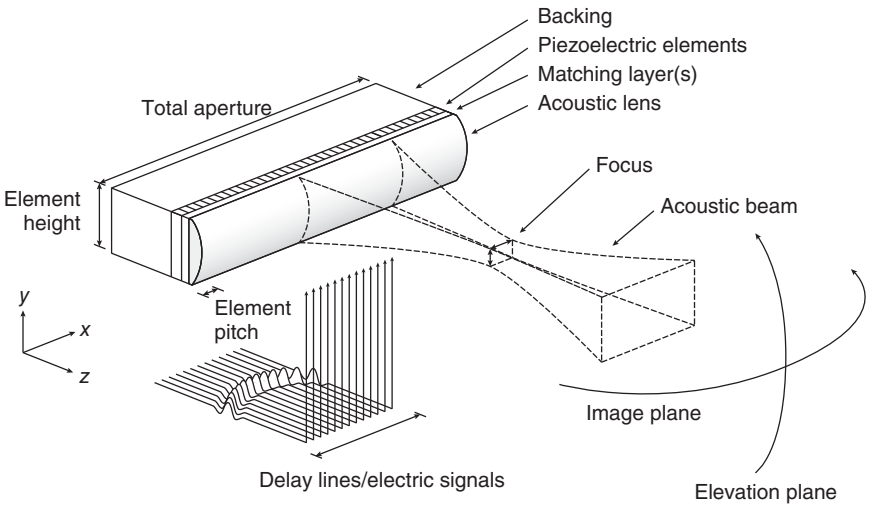


Figure 3.9 Linear phased-array probe using apodization to excite the array with a partial aperture. By controlling the delay of each signal, the system can dynamically move the focus in transmission.

is complicated due to convex shape of the surface. Therefore, most transducers incorporate an acoustic lens. Acoustic lenses are the mechanical analog for optical. They can be fabricated using several techniques, which we have classified into refractive, diffractive, reflective, resonant, and holographic.

3.6.1 Refraction by Bulky Lenses

A wavefront traveling through a flat interface between two materials with different sound speeds will be refracted following Snell's law. When this surface is curved, the wavefront can be collimated to a given point or area, and different curvature strategies can be used to shape the resulting beam profile.

3.6.1.1 Spherical Lenses

For example, a plane wave traveling through a concave lens with *spherical* curvature results in focusing when the sound speed of the lens material, c_m, is higher than the sound speed of the surrounding medium, c_0. When the sound speed of the lens is slower than the medium, $c_m <_c 0$, a convex profile can be used to focus the beam, as shown in Figure 3.10.

The geometrical focus of the beam, F, is given be the refraction index as [26]

$$F = \frac{R}{1 - c_0/c_m} \tag{3.44}$$

where R is the radius of curvature of the spherical lens. However, spherical lenses are not perfect and result in geometric aberrations, which are important for large apertures.

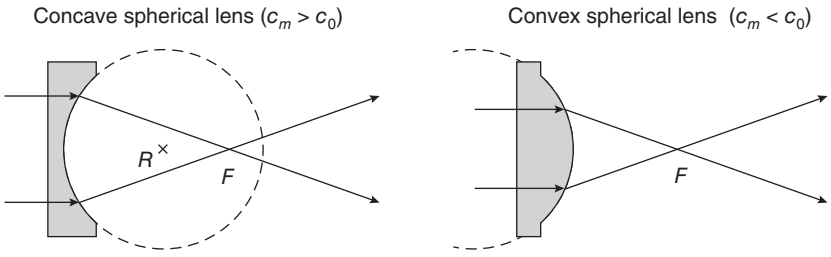


Figure 3.10 Spherical acoustic lenses.

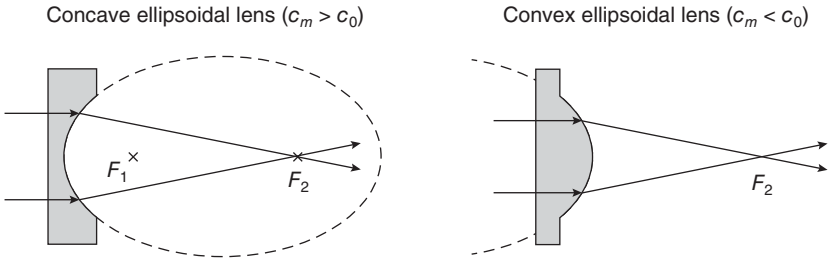


Figure 3.11 Ellipsoidal acoustic lenses.

3.6.1.2 Ellipsoidal Lenses

In this case, a better solution to focus on a point is given by an *ellipsoidal* lens, being the larger focus of the ellipsoid the geometrical focus of the acoustic lens.

In this case, the ellipsoidal lens is designed by setting [27, 28]

$$\epsilon = \frac{c_0}{c_m} \tag{3.45}$$

as the eccentricity of the lens, and the focal spot is generated around the second focus of the ellipse F_2, as shown in Figure 3.11. Aspherical lenses, in analogy with optics, can also be designed. Refractive lenses are usually included in most transducers designs, from medical imaging probes to industrial sensors.

3.6.1.3 Axicon Lenses

Other strategy is to produce a conical wavefront instead of a focused one by using a conical lens, named *axicon* [29, 30]. Axicons can be convex (conical) or concave, as shown in Figure 3.12, as a function of the sound speed ratio c_0/c_m. Instead of a focused beam, axicons generate a (truncated) Bessel beam, i.e. a beam showing a large focal spot with a good lateral resolution.

For moderately focused axicons, the focal length of the Bessel beam F_2, as shown in Figure 3.12, is given by

$$F_2 = \frac{a}{(c_m/c_0 - 1)\alpha} \tag{3.46}$$

where a is the half aperture of the lens, and α is the conical angle of the axicon with respect to the perpendicular plane of the lens. While Bessel beams can be generated

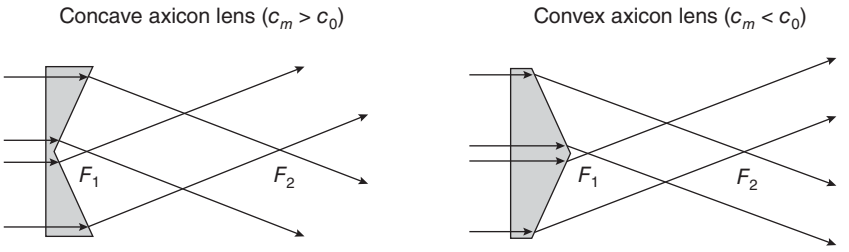


Figure 3.12 Axicon acoustic lenses.

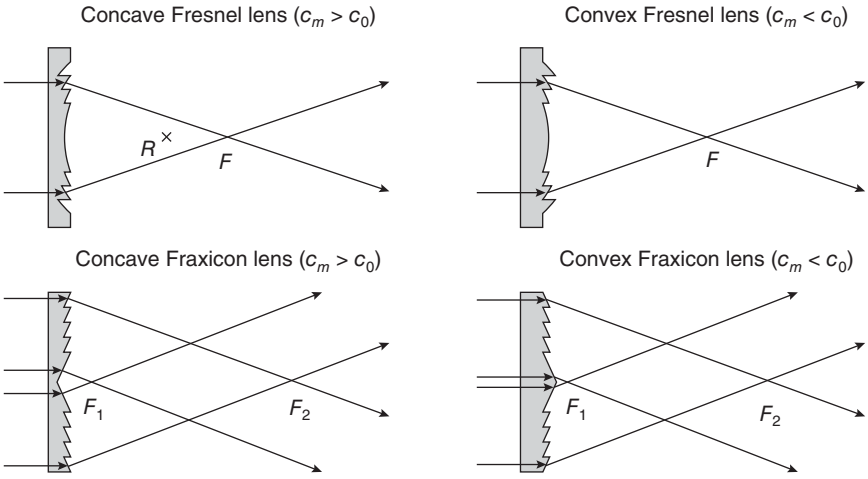


Figure 3.13 Fresnel and fraxicon acoustic lenses.

by annular phased-array sources [31], axicon lenses allow the generation of these limited diffraction beams in a low-cost manner.

3.6.1.4 Frensel and Fraxicon Lenses

Refractive acoustical lenses are bulky when a large aperture and short focal, i.e. large f-number given by $2a/F$, or large gain is required. In this case, the wave should travel through a thick material layer and ultrasound suffers from strong absorption, that can heat and damage the transducer elements. To solve this problem, *Frensel* lenses can be used for focused beams [32], as shown in Figure 3.13. This procedure produces a blazed profile of concave or convex surfaces, resulting in a rough but thin lens. In analogy, *fraxicon* lenses can be designed for Bessel beam generation [33], these lenses presenting a sawtooth radial profile.

3.6.1.5 Lenses for Vortex Generation

In addition, other exotic beams can also be generated using refractive lenses, such as vortex beams. Vortex beams are wavefronts containing a phase dislocation, typically at the beam axis. The phase of the field twists around this phase singularity, and resembling an acoustical whirlpool. At the axis, the field is null due to destructive

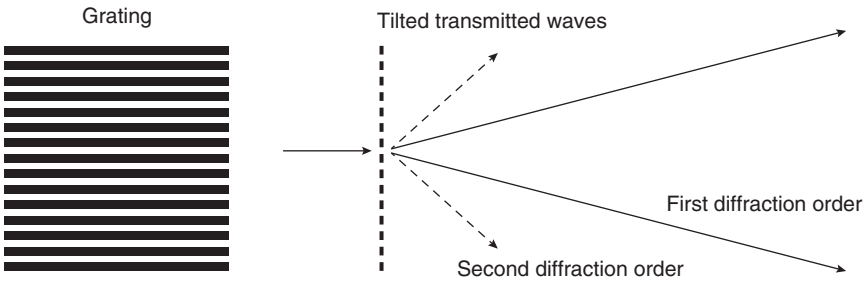


Figure 3.14 Diffraction grating over a period set of apertures, waves are diffracted at angles θ_n.

interference and, therefore, the focal spot of a vortex beam shows a toroidal shape instead of an elliptical one. To generate such a complex beams, one can produce spiral Fresnel lenses or spiral fraxicons [33], e.g. manufacturing them by three-dimensional (3D)-printing techniques. Helicoidal surfaces can also be used [34]. These beams can be used for many biomedical applications such as particle trapping, manipulation, and imaging.

3.6.2 Diffraction by Gratings

Another mechanism to modulate a wavefront is to use the diffraction over an engineered grating. A grating should be highly reflecting to enhance scattering and block the passage of waves in given areas.

3.6.2.1 Cartesian Diffraction Grating

For example, if a set of linear apertures or slits are set on a perfectly reflecting plate, due to the continuity of the transverse wavevector at the interface, ultrasound is transmitted only at particular angles, as shown in Figure 3.14.

These angles, θ_n, are given by

$$\theta_n = \arccos\left(n\frac{\lambda}{d}\right) \tag{3.47}$$

where $n = 0,1,2,\ldots$ is the diffraction grating order, $\lambda = c_0/f$, and a is the separation distance of the slits. We can see that the diffraction grating angles are chromatic, as they depend on frequency. In addition, θ_n only take real values for $|n\lambda/d| \leq 1$, meaning that higher diffraction grating angles only occur in the form of a propagating mode when the slit separation distance d is large compared to the wavelength λ. Using diffraction grating phenomena on axisymmetric geometries one can collimate acoustic beams.

3.6.2.2 Asymmetric Diffraction Grating

When a circular grating is used, as shown in Figure 3.15, by manufacturing a plate with equispaced circular apertures at radial locations [35]. The radial position of each aperture is given by

$$r_m = m \cdot d \tag{3.48}$$

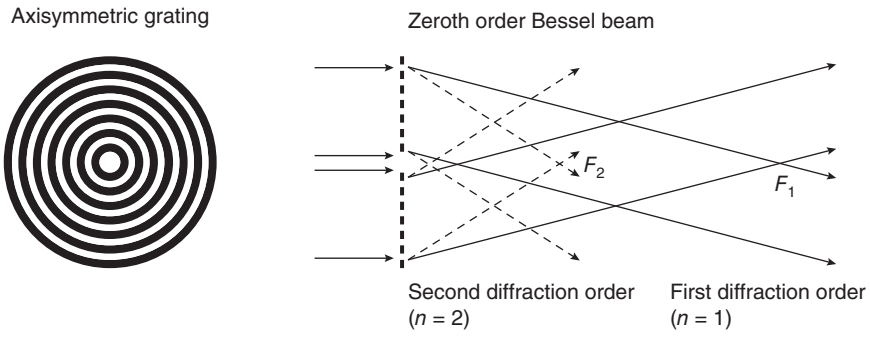


Figure 3.15 Axisymmetric diffraction grating, generates a zeroth-order Bessel beam.

where m is the index of the circular aperture, and d is the separation between them.

Due to asymmetric diffraction grating, a conical wavefront is generated. Its conical angle, α_n, is given for each diffraction grating order n as $\sin\alpha_n = n\lambda/d$. Therefore, and in analogy with axicon lenses, the acoustic field is collimated at the axis in the form of a zeroth-order Bessel beam [35], extending up to a focal distance of

$$F_n = \frac{ad}{n\lambda}\sqrt{1-\left(\frac{n\lambda}{d}\right)^2} \tag{3.49}$$

where a is the half aperture of the lens. We can observe that if higher diffraction orders are excited, they generate secondary elongated focal spots near the source.

3.6.2.3 Fresnel Zone Plates

If a focused beam is desired, then a Fresnel zone plate can be used [36, 37]. The radial location of the mth blocking rings is given by the recursive formula

$$r_{m+1}^2 = r_m^2 + \left(n^2\lambda^2 + n\lambda 2\sqrt{r_m^2 + F^2}\right) \tag{3.50}$$

where F is the focus of the Fresnel zone plate, m is the index of the aperture, and n is the diffraction grating order, as shown in Figure 3.16.

The edge of the mth aperture is given

$$r_m^{2\prime} = \left(\sqrt{r_0^2 + F^2} + m\frac{\lambda}{2}\right)^2 - F^2 \tag{3.51}$$

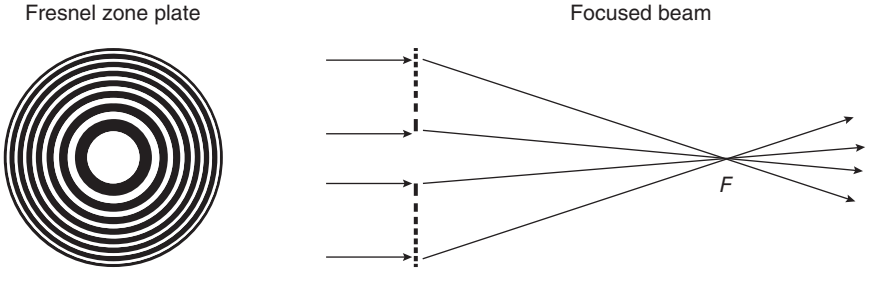


Figure 3.16 Fresnel zone plate produces a focused beam. Only the first diffraction order is shown.

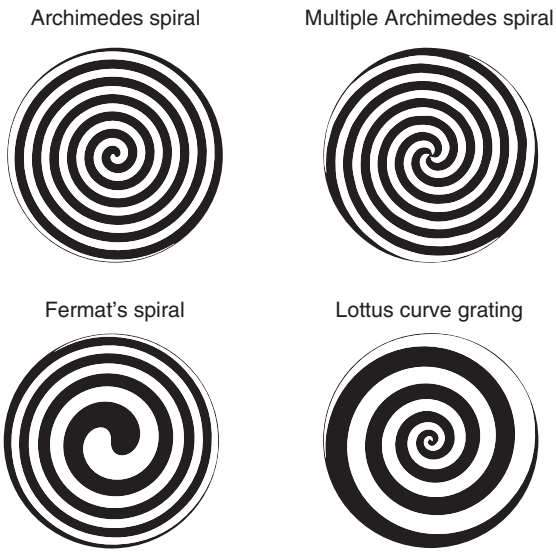


Figure 3.17 Archimedean spiral diffraction gratings. Archimedes spiral generates a high-order vortex beam, multiple arms spirals generate vortices with higher topological charge where the topological charge is proportional to the number of arms. Fermat's spiral produces aberrated focused and the Lottus curve generates unfocused vortex beam.

and the location of the center of each annuls is given by

$$r_m^2 = \left(\sqrt{r_0^2 + F^2} + m\lambda\right)^2 - F^2 \tag{3.52}$$

Diffraction gratings work efficiently only in a limited range of focal distances. For large focal distances, higher diffraction grating orders appear and secondary foci emerge near the source. However, these lenses are easy to manufacture, the designs are simple, and they are stable because they do not depend on the properties of the lens material, only the geometry and the sound speed of the surrounding medium.

3.6.2.4 Archimedean Spiral Gratings

Exotic beams can also be generated using diffraction gratings. For example, the grating can be carved following an Archimedean spiral [38], given by the families of polar curves

$$r(\theta) = \frac{d}{2\pi}\theta^{\gamma} \tag{3.53}$$

The first case is the *Archimedes spiral grating* for $\gamma = 1$. In these spirals the space between winds is constant, given by d, as shown in Figure 3.17.

Therefore, diffraction grating occurs at angles $\sin\alpha_n = n\lambda/d$, like in axisymmetric gratings. However, the phase rotates along the polar coordinate. Therefore, instead of a zeroth-order, a first order Bessel beam is generated [38]. In general, multiple arms spirals generate vortices with higher topological charge where the topological charge is proportional to the number of arms. Higher-order Bessel beams can be generated using Archimedes spiral of multiple arms, as shown in Figure 3.17. Higher diffraction orders also generate high-order Bessel beams.

Vortices can also be generated by Archimedean spirals using $\gamma \neq 1$ see e.g. Ref. 39. Diverging spirals, like the Lottus curve for $\gamma = 2$, can result in a vortex

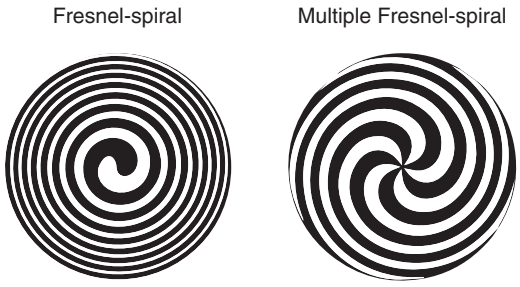


Figure 3.18 Fresnel-spiral zone plate lens, generates a sharply focused vortex beam. The topological charge of the vortex can be controlled using multiple-arm spiral.

beam, but unfocused [40, suppl. mat.]. To generate a focused beam, Archimedean spirals, like the Fermat's spiral for $\gamma = 0.5$, can result in focusing, however, aberrations are produced when focusing vortices using a Fermat's spiral grating [40, suppl. mat.].

3.6.2.5 Fresnel-Spiral Zone Plate

The exact geometrical solution to generate an optimally focused vortex beam the *Fresnel-spiral zone plate* given by the polar curve [40]

$$r_m(\theta)^2 = \left[\sqrt{r_0^2 + F^2} + \lambda\left(\frac{M\theta}{2\pi} - m\right)\right]^2 - F^2 \tag{3.54}$$

where F is the focal of the lens, M is the total number of the arms, m is the index of each arm, and $r_0^2 = (F + \lambda)^2 - F^2$ is the radius of the central opaque area, as shown in Figure 3.18.

In a classical Fresnel zone plate, waves irradiating the zone plate diffract from the opaque zones and constructively interfere at the desired focus. However, in the case of a Fresnel-spiral grating, waves diffracted from opposite angles arrive at the focus in the opposite phase due to the fact that the path difference between both trajectories is $\lambda/2$. Then, in the focal plane, the destructive interference leads to the generation of a hollow focused beam, i.e. a focused vortex beam. One can notice that the Fermat's curve is similar to the Fresnel spiral, but only the Fresnel-spiral curve is the geometrically optimal structure to design binary diffraction gratings producing sharp vortex focusing. Fresnel-spiral using multiple arms allow sharp acoustic focusing, while the topological charge of the vortex beam can be directly related to the number of arms of the Fresnel-spiral. Note that focusing is produced by diffraction grating; therefore, the separation between opaque and transparent areas should be of the order of half wavelength. Thus, the product between the wavenumber and the aperture of the lens should be high enough to allow for various windings.

3.6.3 Reflection by Curved Surfaces

Reflection on curved surfaces can be used to focus an acoustic beam. Shaped by evolution, concave surfaces are present in almost every ear design on living mammals. Spherical acoustic mirrors were used as early warning devices before the World War II, to detect incoming bombers by their engine noise, for example, as those located at the coast of Denge, UK. These concrete mirrors can enhance the sound amplitude at

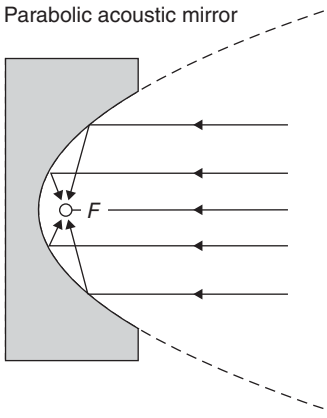


Figure 3.19 Paraboloidal acoustic mirror.

the focal spot. However, spherical mirrors suffer from strong aberrations when they present a large aperture.

3.6.3.1 Parabolic Reflectors

To sharply focus a plane wavefront a better solution than a spherical mirror is to use a parabolic surface, as shown in Figure 3.19. In parabolic mirrors, a plane wave is collimated toward the focus of the paraboloid. Note that, if the wavefront is not plane, then the acoustic focal spot is not sharp and will suffer from aberrations.

These mirrors are used in several acoustic devices. Paraboloids are used in highly directive microphones for acoustics, and also for therapeutic ultrasound applications like extracorporeal shockwave therapy to fragment kidney stones. In this last case, the source is usually a cylindrical electrodynamic transducer.

3.6.3.2 Ellipsoidal Reflectors

Other transducer used for the first designs of lithotriptors for extracorporeal shockwave therapy was an electrohydraulic source, that consists in a spark plug. When the voltage is high enough to break the dielectric, a spark is generated leading to a sudden rise of temperature, creating a collapsing bubble and an intense spherical acoustic wave. However, this diverging wavefront should be focused again on the desired target, the kidney stone.

To focus a spherical wave an ellipsoidal reflector can be used, as shown in Figure 3.20. In this case, the point source should be located on the first focus of the ellipsoid, and the diverging wavefront, after being reflected on the surface, converges to the second focus of the ellipsoid. Note that, in practice, usually truncated ellipsoids are used due to space constraints.

3.6.4 Holograms

3.6.4.1 Field Projections

By using the Helmholtz–Kirchhoff integral, the field produced by an arbitrary complex source can be projected at any point of the space. For example, if the acoustic

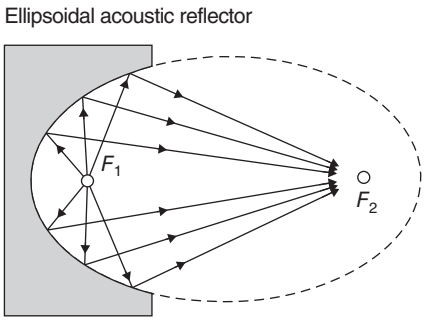


Figure 3.20 Ellipsoidal reflector, focusing a point source located at the first focus of the ellipsoid toward the second one.

field is known in a surface located at a distance $z = z_0$, defined as $P(x, y, z_0)$, we can project that field to another plane located at $z = z_h$, to obtain $P(x, y, z_h)$, as

$$P(x, y, z_h) = -\frac{1}{2\pi} \iint_{-\infty}^{+\infty} \frac{\partial P(x, y, z_0)}{\partial n} \frac{e^{-ikR}}{R} dxdy \tag{3.55}$$

where $R = |\mathbf{r}_h - \mathbf{r}_0|$ is the distance between each point in the original plane, $\mathbf{r}_0 = (x_0, y_0, z_0)$, and each point of the target plane, $\mathbf{r}_h = (x_h, y_h, z_h)$, and $\partial/\partial n = \mathbf{n} \cdot \nabla$ indicates differentiation from the surface normal $\mathbf{n}$. Since $\partial P/\partial n = -ik\rho_0 c_0 v_0$ holds for a plane wave, for a source vibrating at normal speed v_0 Eq. (3.55) results in the Rayleigh–Sommerfeld integral. We can find a more efficient expression for this calculation using the *angular spectrum* of the field, given by as

$$P(k_x, k_y, z) = \iint_{-\infty}^{+\infty} P(x, y, z) e^{-i(k_x x + k_y y)} dxdy \tag{3.56}$$

where k_x and k_y are the transverse components of the wave vector. Note that Eq. (3.56) can be calculated very efficiently using a 2D spatial fast Fourier transform. Thus, we can project the angular spectrum of the source in a z_0 plane onto a z_h plane as

$$P(k_x, k_y, z_h) = P(k_x, k_y, z_0) \cdot H(k_x, k_y, \Delta z) \tag{3.57}$$

where $\Delta z = z_h - z_0$ is the separation distance between planes, and $H(k_x, k_y, \Delta z)$ is the propagator that models the diffraction, given by

$$H(k_x, k_y, \Delta z) = e^{-i\Delta z\sqrt{k^2 - k_x^2 - k_y^2}} \tag{3.58}$$

Using the inverse spatial Fourier transform

$$P(x, y, z) = \frac{1}{4\pi^2} \iint_{-\infty}^{+\infty} P(k_x, k_y, z) e^{i(k_x x + k_y y)} dk_x dk_y \tag{3.59}$$

we can retrieve the field from the angular spectrum as

$$P(x, y, z_h) = \frac{1}{4\pi^2} \iint_{-\infty}^{+\infty} P(k_x, k_y, z_0) e^{-i(k_x x + k_y y)} e^{-i(z_h - z_0)\sqrt{k^2 - k_x^2 - k_y^2}} dk_x dk_y \tag{3.60}$$

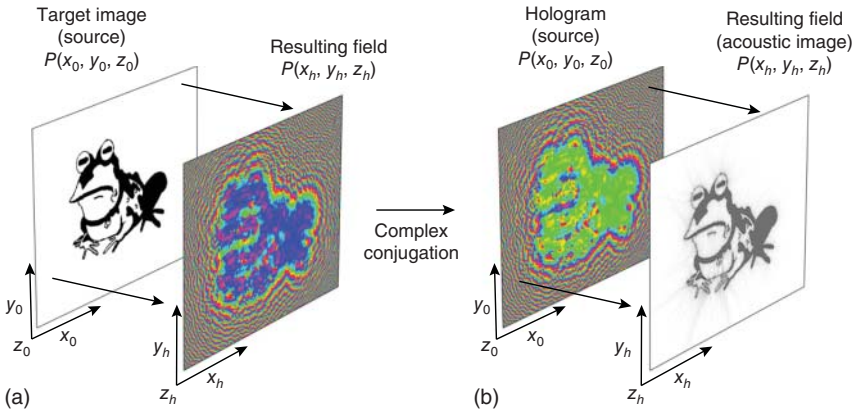


Figure 3.21 (b) Projection process of the field generated by an acoustic source with an arbitrary surface $P(x_0, y_0, z_0)$, in this case an image. At a distance z_h the projected field is given by $P(x_h, y_h, z_h)$. (a) If the source now radiates the complex conjugate of the projected field, at a distance of z_h we reconstruct a diffraction-limited acoustic image, which resembles the original source.

These expressions allow the calculation of a field in one plane from the measurement of the field in another plane. This opens the door to different applications, such as the characterization of the radiation of a source from near-field measurements, known as acoustic holography techniques (Figure 3.21) [41].

3.6.4.2 Synthesis of Acoustic Images

One of the advantages of using these methods is that the field information can be projected both forwards and backwards, which makes it possible to calculate the field produced by a source, but also vice versa, i.e. to know which source would produce a target field. In essence, the time-reversal symmetry of the wave equation allows us the back projection processes. These methods are based on techniques developed in optics by Denis Gabor [42] who discovered that a 3D representation of an object could be obtained from the interference between a reference light beam and the waves reflected by the object. As the pattern of the reflected waves could be printed on a photographic plate, the real object was not needed to reconstruct the virtual image once the wavefront was captured. He called the capturing surface (and not the 3D representation) the *hologram*,[2] and for this he was awarded with the Nobel Prize in Physics in 1971.

Using these optical holograms, light beams can be modulated to generate visible images. In the same way, acoustic holograms can also be used to synthesize acoustic images, i.e. to concentrate sound or vibrations in an arbitrary area of space, and simultaneously allow other areas to remain silent or at rest. Acoustic holograms modify the mechanical wavefront in such a way that they are able to modulate both their phase and, in some cases, their amplitude. For acoustic waves at ultrasonic frequencies, such as those commonly used in biomedical applications around 1 MHz,

2 The word holography comes from the Greek *holos* meaning "complete" and *gram* meaning "drawing."

acoustic holograms can be fabricated by 3D printing elastic polymers, resulting in acoustic lenses with a roughness scale of a few millimeters [43].

3.6.4.3 Biomedical Applications of Holograms

These acoustic holograms have found a recent application in the biomedical field. For example, they have been proposed for targeted ultrasound therapies in neurology [44]. Focused ultrasound is commonly used for multiple neurological therapies, and offers many desirable aspects, as it does not use ionising radiation, resulting in completely noninvasive, safe, and cost-effective treatments. Examples of these treatments are thermal ablation of thalamic nuclei by focused ultrasound for the treatment of essential tremor, opening the blood-brain barrier for localized and noninvasive drug delivery, or focal neuromodulation applications by mechanical action of ultrasound on central nervous system tissues. However, on their way to the brain, ultrasound beams are affected by aberrations introduced by skull bones, which introduce strong attenuation and refraction by irregularly modifying the wavefront. Aberration and refraction results in a poor and uncontrolled focusing. Moreover, in many cases the area of therapeutic interest is not a single point, but a structure with a particular 3D shape, as occurs in therapies on deep brain nuclei, e.g. the hippocampus. Acoustic holographic lenses can overcome these limitations. Since holograms offer very precise manipulation of the wavefront, low-cost 3D printed holographic lenses can be designed to compensate for aberrations introduced by bones and, simultaneously, focus mechanical energy in an arbitrary area, e.g. they can generate several focal points, allowing several structures of the central nervous system to be targeted at the same time. For example, using holograms we can simultaneously open the blood-brain barrier on two spots of the brain, i.e. at the left and right hemispheres [45] (Figure 3.22).

These acoustic holograms go beyond traditional ultrasound beams to synthesize complex acoustic images, allowing the generation of curved or self-bending beams [44], or even focal zones in the shape of the target in the deep-brain using small

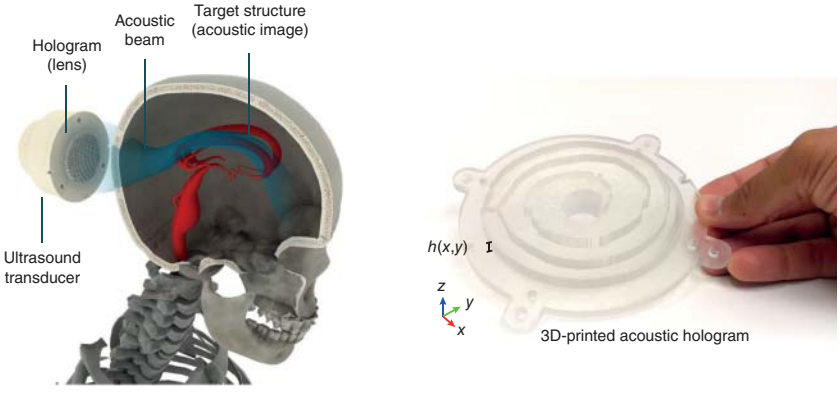


Figure 3.22 Application of acoustic holograms for therapeutic ultrasound in neurology, and example of 3D printed holographic lens. Source: Jimenez-Gamb et al. [46]/American Physical Society.

apertures [47]. Holograms also make it possible to synthesize other complex acoustic fields within the skull, such as vortex beams [46]. These beams have a phase singularity on the axis, which opens the door to noninvasive, noncontact trapping and manipulation of small objects such as drug aggregates or clots within the central nervous system. Beyond neurology, holograms has been also proposed for large volume hyperthermia [48]. Holographic lenses open new avenues to generalize emerging applications of therapeutic ultrasound, such as localized drug delivery or neuromodulation procedures, through noninvasive and very low-cost systems.

References

1 Curie, J. and Curie, P. (1880). Développement par compression de l'électricité polaire dans les cristaux hémièdres à faces inclinées. *Bulletin de minéralogie* 3 (4): 90–93.

2 Kino, G.S. (1987). *Acoustic Waves: Devices, Imaging, and Analog Signal Processing*. Englewood Cliffs, NJ: Prentice-Hall.

3 Arnau, A. (2008). *Piezoelectric Transducers and Applications*, *Springer Science & Business Media*. Berlin, Heidelberg: Springer-Verlag.

4 Krimholtz, R., Leedom, D.A., and Matthaei, G.L. (1970). New equivalent circuits for elementary piezoelectric transducers. *Electronics Letters* 6 (13): 398–399.

5 Liu, Z., Wu, H., Ren, W., and Ye, Z.-G. (2022). Piezoelectric and ferroelectric materials: fundamentals, recent progress, and applications. In: *Reference Module in Chemistry, Molecular Sciences and Chemical Engineering*. Elsevier. ISBN 978-0-12-409547-2. https://doi.org/10.1016/B978-0-12-823144-9.00069-8. https://www.sciencedirect.com/science/article/pii/B9780128231449000698.

6 Chilibon, I. and Marat-Mendes, J.N. (2012). Ferroelectric ceramics by sol–gel methods and applications: a review. *Journal of Sol-Gel Science and Technology* 64 (3): 571–611.

7 Tressler, J.F., Alkoy, S., and Newnham, R.E. (1998). Piezoelectric sensors and sensor materials. *Journal of Electroceramics* 2 (4): 257–272.

8 Panda, P.K. (2009). Environmental friendly lead-free piezoelectric materials. *Journal of Materials Science* 44 (19): 5049–5062.

9 Rathod, V.T. (2020). A review of acoustic impedance matching techniques for piezoelectric sensors and transducers. *Sensors* 20 (14): 4051.

10 Fukada, E. (2000). History and recent progress in piezoelectric polymers. *IEEE Transactions on Ultrasonics, Ferroelectrics, and Frequency Control* 47 (6): 1277–1290.

11 Xie, L., Wang, G., Jiang, C. et al. (2021). Properties and applications of flexible poly(vinylidene fluoride)-based piezoelectric materials. *Crystals* 11 (6): 644.

12 Akdogan, E.K., Allahverdi, M., and Safari, A. (2005). Piezoelectric composites for sensor and actuator applications. *IEEE Transactions on Ultrasonics, Ferroelectrics, and Frequency Control* 52 (5): 746–775.

13 Inoue, T., Ohta, M., and Takahashi, S. (1987). Design of ultrasonic transducers with multiple acoustic matching layers for medical application. *IEEE Transactions on Ultrasonics, Ferroelectrics, and Frequency Control* 34 (1): 8–16.

14 Alvarez-Arenas, T.E.G. (2004). Acoustic impedance matching of piezoelectric transducers to the air. *IEEE Transactions on Ultrasonics, Ferroelectrics, and Frequency Control* 51 (5): 624–633.

15 Desilets, C.S., Fraser, J.D., and Kino, G.S. (1978). The design of efficient broad-band piezoelectric transducers. *IEEE Transactions on Sonics and Ultrasonics* 25 (3): 115–125.

16 Fang, H.J., Chen, Y., Wong, C.M. et al. (2016). Anodic aluminum oxide–epoxy composite acoustic matching layers for ultrasonic transducer application. *Ultrasonics* 70: 29–33.

17 Kossoff, G. (1966). The effects of backing and matching on the performance of piezoelectric ceramic transducers. *IEEE Transactions on Sonics and Ultrasonics* 13 (1): 20–30.

18 King, L.V. (1934). On the acoustic radiation field of the piezo-electric oscillator and the effect of viscosity on transmission. *Canadian Journal of Research* 11 (2): 135–155. https://doi.org/10.1139/cjr34-080.

19 Douglas Mast, T. and Yu, F. (2005). Simplified expansions for radiation from a baffled circular piston. *The Journal of the Acoustical Society of America* 118 (6): 3457–3464. https://doi.org/10.1121/1.2108997.

20 O'Neil, H.T. (1949). Theory of focusing radiators. *The Journal of the Acoustical Society of America* 21 (5): 516–526. https://doi.org/10.1121/1.1906542.

21 Lucas, B.G. and Muir, T.G. (1982). The field of a focusing source. *The Journal of the Acoustical Society of America* 72 (4): 1289–1296. https://doi.org/10.1121/1.388340.

22 Chen, X., Schwarz, K.Q., and Parker, K.J. (1993). Radiation pattern of a focused transducer: a numerically convergent solution. *The Journal of the Acoustical Society of America* 94 (5): 2979–2991. https://doi.org/10.1121/1.407329.

23 Makov, Y.N., Espinosa, V., Sánchez-Morcillo, V.J. et al. (2006). Strong on-axis focal shift and its nonlinear variation in low-Fresnel-number ultrasound beams. *The Journal of the Acoustical Society of America* 119 (6): 3618–3624. https://doi.org/10.1121/1.2197805.

24 Camarena, F., Adrián-Martínez, S., Jiménez, N., and Sánchez-Morcillo, V. (2013). Nonlinear focal shift beyond the geometrical focus in moderately focused acoustic beams. *The Journal of the Acoustical Society of America* 134 (2): 1463–1472. https://doi.org/10.1121/1.4812865.

25 Jiménez, N., Camarena, F., and González-Salido, N. (2017). Dynamic nonlinear focal shift in amplitude modulated moderately focused acoustic beams. *Ultrasonics* 75: 106–114.

26 Fry, W.J. and Dunn, F. (1962). Ultrasound: analysis and experimental methods in biological research. In: Nastuk, W.L. *Physical Techniques in Biological Research. IV. Special Methods*, Academic Press Inc.: New York City 261–394.

27 Schlussler, L. (1980). The design and test results for an acoustic lens with elliptic surfaces. *The Journal of the Acoustical Society of America* 67 (2): 699–701.

28 Dunn, F. and Fry, F.J. (1980). Acoustic elliptic lenses: a historical note. *The Journal of the Acoustical Society of America* 68 (1): 350.

29 McLeod, J.H. (1954). The axicon: a new type of optical element. *JOSA* 44 (8): 592–597.

30 Burckhardt, C.B., Hoffmann, H., and Grandchamp, P.-A. (1973). Ultrasound axicon: a device for focusing over a large depth. *The Journal of the Acoustical Society of America* 54 (6): 1628–1630.

31 Hsu, D.K., Margetan, F.J., and Thompson, D.O. (1989). Bessel beam ultrasonic transducer: fabrication method and experimental results. *Applied Physics Letters* 55 (20): 2066–2068.

32 Hadimioglu, B., Rawson, E.G., Lujan, R. et al. (1993). High-efficiency Fresnel acoustic lenses. *1993 Proceedings IEEE Ultrasonics Symposium*, 579–582. IEEE.

33 Jiménez-Gambín, S., Jiménez, N., Benlloch, J.M., and Camarena, F. (2019). Generating Bessel beams with broad depth-of-field by using phase-only acoustic holograms. *Scientific Reports* 9 (1): 1–13. https://doi.org/10.1038/s41598-019-56369-z.

34 Jiménez, N., Ealo, J., Muelas-Hurtado, R.D. et al. (2021). Sub-wavelength acoustical vortex beams using self-demodulation. *Physical Review Applied* 15 (5): 054027. https://doi.org/10.1103/PhysRevApplied.15.054027.

35 Jimenez, N., Romero-García, V., Picó, R. et al. (2014). Acoustic Bessel-like beam formation by an axisymmetric grating. *EPL (Europhysics Letters)* 106 (2): 24005.

36 Farnow, S.A. and Auld, B.A. (1974). Acoustic Fresnel zone plate transducers. *Applied Physics Letters* 25 (12): 681–682.

37 Jimenez, N., Romero-García, V., Pico, R. et al. (2015). Nonlinear focusing of ultrasonic waves by an axisymmetric diffraction grating embedded in water. *Applied Physics Letters* 107 (20): 204103.

38 Jiménez, N., Picó, R., Sánchez-Morcillo, V. et al. (2016). Formation of high-order acoustic Bessel beams by spiral diffraction gratings. *Physical Review E* 94 (5): 053004.

39 Wang, T., Ke, M., Li, W. et al. (2016). Particle manipulation with acoustic vortex beam induced by a brass plate with spiral shape structure. *Applied Physics Letters* 109 (12): 123506. https://doi.org/10.1063/1.4963185.

40 Jiménez, N., Romero-García, V., García-Raffi, L. et al. (2018). Sharp acoustic vortex focusing by Fresnel-spiral zone plates. *Applied Physics Letters* 112 (20): 204101.

41 Maynard, J.D., Williams, E.G., and Lee, Y. (1985). Nearfield acoustic holography: I. Theory of generalized holography and the development of NAH. *The Journal of the Acoustical Society of America* 78 (4): 1395–1413.

42 Gabor, D. (1948). A new microscopic principle. *Nature* 161: 777–778.

43 Melde, K., Mark, A.G., Qiu, T., and Fischer, P. (2016). Holograms for acoustics. *Nature* 537 (7621): 518–522.

44 Jiménez-Gambín, S., Jiménez, N., Benlloch, J.M., and Camarena, F. (2019). Holograms to focus arbitrary ultrasonic fields through the skull. *Physical Review Applied* 12 (1): 014016.

45 Jiménez-Gambín, S., Jiménez, N., Pouliopoulos, A.N. et al. (2022). Acoustic holograms for bilateral blood-brain barrier opening in a mouse model. *IEEE Transactions on Biomedical Engineering* 69 (4): 1359–1368. https://doi.org/10.1109/TBME.2021.3115553.

46 Jiménez-Gambín, S., Jiménez, N., and Camarena, F. (2020). Transcranial focusing of ultrasonic vortices by acoustic holograms. *Physical Review Applied* 14 (5): 054070. https://doi.org/10.1103/PhysRevApplied.14.054070.

47 Andrés, D., Jiménez, N., Benlloch, J.M., and Camarena, F. (2022). Numerical study of acoustic holograms for deep-brain targeting through the temporal-bone window. *Ultrasound in Medicine and Biology* 48 (5): 872–886. https://doi.org/10.1016/j.ultrasmedbio.2022.01.010.

48 Andrés, D., Vappou, J., Jiménez, N., and Camarena, F. (2022). Thermal holographic patterns for ultrasound hyperthermia. *Applied Physics Letters* 120 (8): 084102. https://doi.org/10.1063/5.0081565.